nature communications

Article

https://doi.org/10.1038/s41467-025-66587-x

State-correlated reaction dynamics unveiled in full from a single product-image measurement

Received: 17 July 2025

Accepted: 6 November 2025

Published online: 25 November 2025

Check for updates

Huilin Pan[1,2,5] ✉, Shu Liu[1,5] ✉, Pengcheng Wang[1,5], Xueming Yang[1,2] ✉, Dong H. Zhang[1] ✉ & Kopin Liu[1,3,4]

Electron- or photoionization mass spectrometry coupled with product time-of-flight measurement is a universal detection scheme, which has been playing pivotal role in advancing our fundamental understanding of chemical reactions. This powerful detection scheme, however, usually does not provide the product state-specific information. Here, we propose a variant of universal detection with state-resolving capability by leveraging a three-dimensional velocity-map imaging detector with vacuum-ultraviolet photoionization probe. As demonstrated by a crossed-beam reaction of $F + CH_4 \rightarrow CH_3(v_i) + HF(v)$, both product vibrational branching and state-resolved angular distributions are simultaneously unveiled in a (v_i, v) pair-correlated manner from a single product-image measurement, which enables us to gain previously inaccessible insights. Comparisons with a six-dimensionality quantum dynamics calculation show excellent agreements, validating the approach. The proposed method is general and should open a new opportunity to gain deeper insights into many important complex chemical processes that are otherwise difficult to study.

One of the fundamental goals of physical chemistry is to understand how a chemical transformation that invokes the breaking and forming of chemical bonds takes place. Reaction dynamics addresses this question from the molecular point of view, i.e., how the constituent atoms rearrange themselves in going from reactants to products[1,2]. The knowledge of product state and angular distributions has proven insightful in advancing our current understanding of chemical reactivity over the past decades. For instance, a statistical product state distribution and forward-backward symmetric angular distribution will strongly suggest an indirect complex-forming mechanism with a long-lived reaction intermediate[3], whereas a non-statistical formation of a highly inverted product vibrational state distribution (or a hot translational energy release), usually accompanied by very anisotropic angular distributions, will be the imprint of a direct mechanism with the activated barrier lying early (or late) along the reaction pathway[4].

Traditionally, two distinct experimental approaches have been developed to acquire such dynamical attributes. For the simple atom + diatom reaction, state-resolved detection of the diatomic product by laser spectroscopy, if applicable, suffices. Complex reactions, however, can lead to multiple product channels and often yield polyatomic products, whose detailed spectroscopic information, in most cases, might not be available. Then, a universal detection using either electron-impact[5–7] or non-resonant one-photon ionization[8–10] mass spectroscopic scheme becomes the method of choice. The time-of-flight measurements of the (neutral) products in this approach typically yield broad, featureless kinetic energy distributions, thus providing no product state information, except for the landmark work on

[1]State Key Laboratory of Chemical Reaction Dynamics, Dalian Institute of Chemical Physics, CAS Dalian, P. R. China. [2]Department of Chemistry, Southern University of Science and Technology, Shenzhen, P. R. China. [3]Aerosol Science Research Center, National Sun Yat-sen University, Kaohsiung, Taiwan. [4]Institute of Atomic and Molecular Sciences (IAMS), Academia Sinica, Taipei, Taiwan. [5]These authors contributed equally: Huilin Pan, Shu Liu, Pengcheng Wang. ✉e-mail: panhl2019@sustech.edu.cn; liushu1985@dicp.ac.cn; xmyang@dicp.ac.cn; zhangdh@dicp.ac.cn

$F + H_2$ and its isotopic variants[11]. In other words, this general-purpose method trades the state-specificity for its universality—a dilemma of "seeing the forest but not trees". Consequently, these two conventional approaches are generally conceived of applying to different classes of reactions depending on the availability of product spectroscopy.

Moreover, a polyatomic reaction often yields two molecular products. Then, even if the spectroscopic prerequisite of one product is fulfilled, the conventional spectroscopic methods would remain blind to the internal-state distributions of its coproduct. In order to uncover such a hidden information, a method combining the resonance-enhanced multiphoton ionization (REMPI) spectroscopy with high-resolution velocity map of the REMPI-tagged ions was developed[12] to acquire, with the aid of energy and momentum conservations, the state-correlation between the concomitantly formed product pair in each individual reactive event[13,14].

Despite the advance of this innovative method, the detailed information thus derived still suffers a significant shortcoming of being fragmentary, making it cumbersome to piece that information together for a bigger picture—a crucial aspect needed for a deeper understanding of chemical reactivity. As previously reported on the $F + CD_4$ reaction, the umbrella-mode (υ_2) excited products $CD_3(\upsilon_2 = 0, 1, 2, 3)$ were individually REMPI-tagged and imaged to reveal the concomitantly formed DF vibrational states of each individual $CD_3(\upsilon_2)$ state—one at a time[13,15]. The resultant pair-correlated distribution of ($\upsilon_{2(CD3)}$, υ_{DF}), however, bore notable uncertainties of the relative REMPI detection sensitivities of each individually interrogated $CD_3(\upsilon_2)$ state. [The notation of ($\upsilon_{2(CD3)}$, υ_{DF}) refers to the vibrational quantum states of two products, CD_3 and DF, that are concomitantly formed in a single reactive event.] In addition, the information on other modes of excitation of CD_3 was missing for either the lack of spectroscopic data or the weakness of REMPI signals, which, however, not necessarily reflects low reactivity. A similar experiment on the individual pair-correlated angular distribution of ($\upsilon_{2(CH3)}$, υ_{HF}) in $F + CH_4$ was recently reported; though no attempt was made to obtain the pair-correlated vibrational branching[16]. Therefore, it is most pressing to develop an alternative detection scheme with two seemingly conflicting requirements of universality and state-specificity to quantitatively delineate the fuller picture of the reactivity.

In this work, we propose a general detection method with both universal and state-specific capabilities. We demonstrate, using the benchmark $F + CH_4$ reaction, that complete product state and angular distributions can be simultaneously acquired in a pair-correlated manner from a single measurement, rendering more robust results possible without problematic calibrations of the detection sensitivities of different states by other state-specific methods. To attest the reliability of the experimental results, we also perform quantum dynamics calculation on a highly accurate full-dimensional potential energy surface. The comparisons between experiment and theory show remarkable agreements in nearly all aspects. Furthermore, the uncovered dynamical features enable us to pinpoint the angle–angular momentum correlation being the key factor in governing the reactivity.

Results

A universal detection with product state-specificity

We achieved that by fully utilizing the unique feature of (ion) velocity-map imaging (VMI) of the recoiled products in a three-dimensional (3D) manner (Methods, Supplementary Fig. 1). By exploiting vacuum ultraviolet (VUV) one-photon ionization as a general probe, the widely used 2D image technique velocity-mapped those (ionized) products in the image plane *x*-*y*—regardless of their spatial locations of (x, y)—to a single spot on a position-sensitive detector[17]. By operating VMI under the soft-focusing condition (17.6 V/cm extraction field), the arrival time of the whole ion packet was stretched to about 300 ns, and at the same time, the temporal spreads of those ions with the same v_z-speed but residing at different locations along the *z*-direction were greatly compressed through the space-focusing effect[12,18,19]. As such, the acquired imaging signals become insensitive to the finite scattering and ionization volumes, and thus the full product 3D velocity information can be faithfully mapped out.

The reaction of $F + CH_4 \rightarrow CH_3 + HF$ was benchmarked for proof-of-concept demonstration. This reaction has been the subject of extensive studies over the past decades for its fundamental significance as a prototypical polyatomic reaction as well as its practical application in chemical lasers[20–27]. Dynamically, most of the prior works focused on the product state distributions of either CH_3 or HF (refs. 23–26), except for more recent studies on the angular distributions through REMPI-tagged product pair-correlation measurements[13–16]. In this work, we used 118 nm (10.48 eV) photons to ionize CH_3 products (ionization potential of 9.84 eV). One-photon ionization scheme has previously been employed in numerous studies of polyatomic reactions; no state-resolved features have ever been reported[8–10]. The implementation of the above 3D-VMI scheme, combined with time-sliced imaging (<20 ns gate-width) detection of the 3D velocity information of CH_3^+ at the center of the ion packet[12], enables us to reveal all possible states of concomitantly formed product pairs of CH_3 and HF. As will be presented below, the results from such universal and state-specific detection in turn give access to hitherto inaccessible information.

It has been shown that over the photon energy range of 10.2——11 eV, the CH_3 photoionization cross-section appears to be independent of the umbrella-mode vibrational level (up to $\upsilon_2 = 2$)[28–31]. This vibrational independency can be ascribed to the non-bonding nature of the highest-occupied molecular orbital (HOMO) of the CH_3 ground state and structural resemblance of the final CH_3^+ state. Consequently, the Franck-Condon envelopes for photoionization would strongly favor the transitions that preserve both the vibrational mode and its quantum number[28,30]. Furthermore, because the 118 nm photon energy lies 0.64 eV above the ionization threshold, thus exceeding the autoionization regime, no strong vibrational dependence is expected. Thereby, we surmised that the present ionization scheme could serve as a universal probe with nearly uniform detection efficiency for the ro-vibrational states of CH_3 products of our concern.

All essential dynamical attributes from a single image

Figure 1A presents the background-subtracted raw image of one-photon ionized CH_3 products in the $F + CH_4$ reaction at collision energy (E_c) of 2.4 kcal mol^{-1} (0.106 eV), for which the photochemical and discharge-generated spurious backgrounds have been subtracted (Supplementary Fig. 2). The distributions of previously reported (0_0, 3) and (0_0, 2) product pairs, obtained by REMPI-tagged ground-state $CH_3(0_0)$ products[32], are clearly seen as labels *b* and *h*, respectively. Lying between them are a series of new ring-like features. Also shown in Fig. 1C are the relevant energetics of all product vibrational pairs (υ_{CH3}, υ_{HF}) of this work. Based on energy conservation, the nature of those ring-like features can readily be identified and assigned in red in Fig. 1C. Significantly, the vibrational excitation of CH_3 products reside predominantly in the umbrella-mode (υ_2), with minor production of symmetric-stretching (υ_1) excitation and nearly null in the remaining modes of υ_3 (asymmetric stretch) and υ_4 (deformation)—clearly, a highly mode-selective reaction. The formation of $CH_3(\upsilon_1 = 1)$ has been noted previously in a REMPI-tagged VMI experiment[33]. However, its relative reactivity could not be quantified at the time due to the unknown relative REMPI detection sensitivity of the 1_1^1-band.

The dynamics information encoded in Fig. 1A can be quantified after the density-to-flux correction[12]. Figure 2A presents the resultant product speed distribution P_u over the 0°——90° angular range, where the multiple rings are better resolved. Also shown are two sparse features shaded in pink, which are the speed distributions of (0_0, 3) and

https://doi.org/10.1038/s41467-025-66587-x

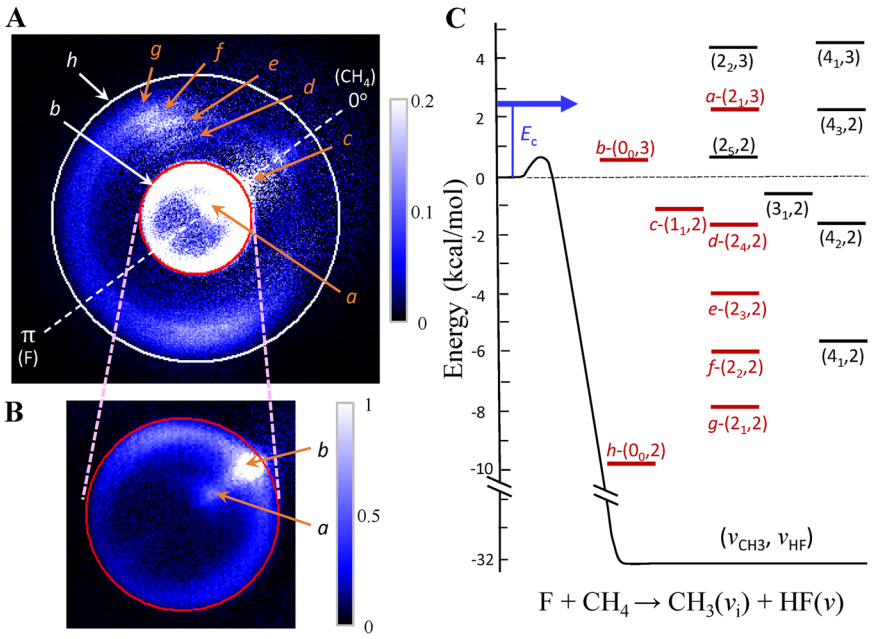

Fig. 1 | Product image and relevant energetics. A Background-subtracted raw image of CH_3 products in the reaction of F + CH_4 at E_c = 2.4 kcal mol^{-1}, which was deduced from subtracting the photochemical background of CH_4 reactants and the discharge-generated background (see Supplementary Fig. 2). The directions of two reactant beams in the center-of-mass coordinate are also indicated for clarity. Numerous ring-like features are revealed and labeled as *a*, *b*,.... *h*. A red circle and a white one indicate the speed limits for features *b* and *h*, respectively. **B** An expanded view of two inner-most features *a* and *b*. The color bars in (**A**, **B**) show the relative intensity, respectively. **C** The energy-level structures of the vibrational product pairs of (v_{CH3}, v_{HF}) relevant to this work; as an example, the notation of (2_1, 3) indicates one-quantum excitation of the v_2 mode of CH_3 and three quanta excitation of HF vibration. The combination bands of the CH_3 radical are not considered here because of presumably small populations. All observed image features in (**A**) can be identified by conservation of energy as the product pairs marked in red.

(0_0, 2) acquired previously from an image with λ-scanning the Q-head of $CH_3(0_0^0)$ REMPI band[32]. As seen, both peaks match very well with the features *b* and *h*, respectively. Note a nearly symmetric profile of the (0_0, 3) pair and an asymmetric one with a long tail toward slower speeds for (0_0, 2). Presumably, such distinct shapes reflect that more energy is available for disposal into the two rotors (CH_3 and HF) of the (0_0, 2) vibrational pair. By subtracting the pink-shaded distribution from the present P_u, the speed distributions of vibrationally excited $CH_3(v_i)$ products are unveiled in Fig. 2B. Based on the energetic onset of each product pair (Fig. 2A) and referred to the extended tails of the (0_0, 3) and (0_0, 2) distributions, the profile of each individual vibrationally excited pair was then estimated and dissected from the congested distribution. The results are displayed as the blue dotted line in Fig. 2B. Once the shape of each component was determined, the product speed and translational energy distributions over the full angular range could then be uncovered by varying the magnitude of each individual vibrational component, while keeping its shape intact, till the observed total distributions were fitted. The results are presented in Fig. 2C, D, respectively.

Figure 3A summarizes the (pair) correlated vibrational branching fraction deduced from Fig. 2C or Fig. 2D in a 3D (v_{CH3}, v_{HF})-matrix representation. We also perform a reduced six-dimensionality (6D) state-to-state quantum dynamics (QD) calculation[34] on a highly accurate full-dimension neural network (NN) potential energy surface[35]. The 6D model (Methods: Theory) first constrains the nonreacting CH_3 group within the C_{3V} symmetry based on the eight-dimensional (8D) framework of Palma and Clary[36], and then assumes that the CH_3 group can rotate freely around its C_{3V} symmetry axis and the CH bond length can be fixed at its equilibrium value in the reactant (2.06 bohr) to further reduce computational costs. Test calculations show that the 6D treatment yields reaction probabilities in good agreement with those of the 8D treatment. After including the effects of initial CH_4 rotational states of this experiment at 8 K (Methods: Experiment), the QD results are displayed in Fig. 3B, for which only the v_2 mode is explicitly considered. Remarkable agreements between experiment and theory are noted in nearly all aspects. For example, although the dominance of umbrella-mode excitation of $CH_3(v_2)$ is intuitively anticipated, both experiment and theory show that the distribution of the v_2-excitations, concomitantly formed with HF(v = 2), peaks around v_2 = 1—a rather mild excitation. Collectively, the umbrella-mode excitations account for ∽58% (theory) to ∽57% (experiment) of total reactive fluxes, an unprecedented and perhaps unexpected finding. Good agreements are also notable from the lower-dimension product state distributions of HF (in red, sum of all concomitantly formed $CH_3(v_i)$ states for a given HF(v) state) and likewise $CH_3(v_i)$ (in blue) displayed on the respective background. Such global agreements not only testify the experimental conjecture of uniform detection efficiencies of all CH_3 internal states, but also validates that key dynamical feature can indeed be faithfully captured by the present theoretical 6D-approximation.

Figure 4 compares the experimental and theoretical correlated differential cross sections (CDCSs) at E_c = 2.4 kcal mol^{-1}. This is the first 6D-QD calculation of state-to-state CDCSs for a six-atom reaction with dynamical resonances. As seen, both display similar patterns showing strikingly distinct distributions for different product pairs. Nearly all product pairs feature a sharp forward structure, for which the theoretical prediction appears significantly sharper. Two plausible mechanisms could account for such distinctive forward peaking: A classical slowing-down (or time-delay) mechanism of trajectories over the centrifugally shifted barrier in large impact-parameter collisions[37], and the contribution from a resonance-mediated pathway that has been suggested as the dominant reaction mechanism at lower E_c, particularly for the formation of HF(v = 3)[33,38]. As shown in Supplementary Fig. 3, the initial CH_4 rotational excitation significantly lowers the HF(v = 3) branching fraction, implicating a negative impact on the resonance pathway. Thereby, the discrepancies in the forward peaks, the imprint of the resonance pathway, would be reduced if the

https://doi.org/10.1038/s41467-025-66587-x

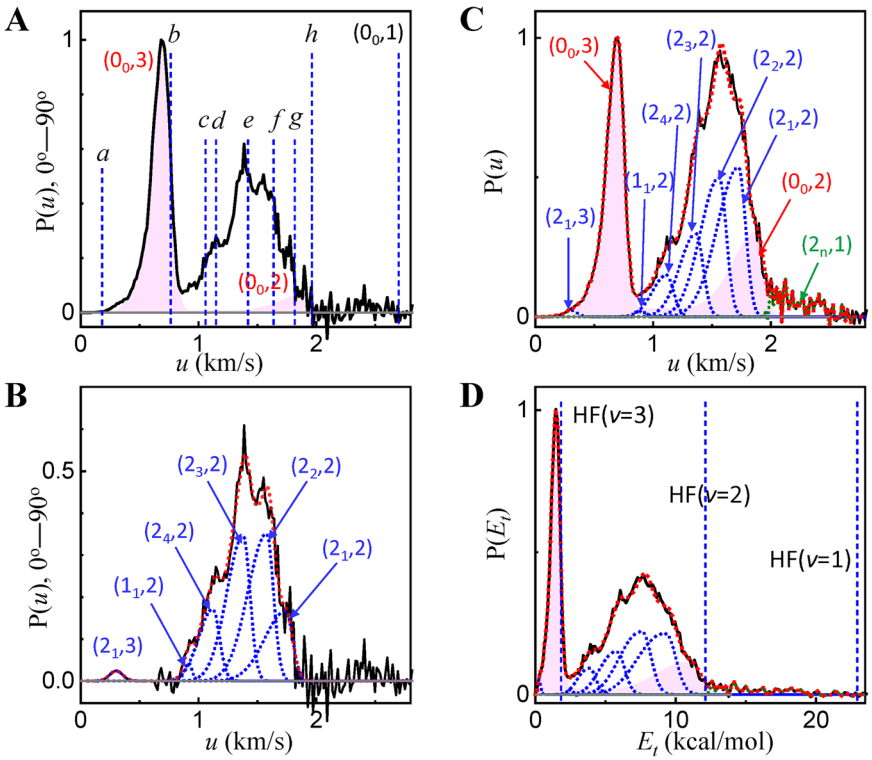

Fig. 2 | Product pair-correlated speed and translational energy distributions. **A** CH_3 product speed distribution over the angular range of 0°——90°, deduced from Fig. 1A after density-to-flux corrections. Two pink-shaded features labeled (0_0, 3) and (0_0, 2) are the corresponding distributions acquired previously from an image with λ-scanning the entire Q-head of the $CH_3(0_0^0)$ REMPI band[32]; thus, all rotational states of two products were probed as the present study. The vertical dotted lines denote the energetic limits of the corresponding features shown in Fig. 1A. **B** The speed distributions of vibrationally excited $CH_3(v_i)$ products after subtracting the pink-shaded distribution from the present P_u (black line) in (**A**). The blue dotted lines are the dissected speed distribution of each individual vibrationally excited pair (v_{CH3}, v_{HF}). The red dotted line is their sum. **C** The CH_3 speed distribution (black line), the pair components (shaded pink for the $CH_3(0_0)$ pairs and blue dotted lines for the vibrationally excited $CH_3(v_i)$ pairs), and the simulated sum in red dotted line over the full angular range. **D** As (**C**), but presented as the distribution of total translational energy release, $P(E)$. For clarity, only the energetic limits for the HF vibrational states are indicated as the vertical dotted lines.

reactants $CH_4(j = 1, 2)$ were also included in the calculation. More significantly, the overall distribution evolves from being predominantly forward peaking for (0_0, 3) to exhibiting marked sideways scattering for (2_2, 2), and then to essentially backward-scattered (0_0, 2). Such a systematic trend follows closely with exoergicity of the product pair (Fig. 1C), with the internally hotter pair recoiled mainly in the forward direction and the least (internally) energetic pair shifted to backward scattering.

Mechanistic origin: angle-angular momentum correlation

Two factors could be at work for this prominent recoil energy dependency of angular distributions. As alluded to earlier, the reaction of F + CH_4 proceeds predominantly by a resonant tunneling mechanism at low $E_c \le 1$ kcal mol^{-1} (ref. 33). At $E_c = 2.4$ kcal mol^{-1} the direct abstraction mechanism prevails with minor contribution from the resonance pathway[32,38–41]. This is a highly exoergic, heavy-light-heavy reaction with a somewhat bent, yet highly fluxional, F–H–C transition-state geometry[35,42]. For a light-atom transfer reaction, both the initial and final orbital angular momenta, **l** and **l′**, are mainly carried by the orbital motions of two heavy particles. On inertial grounds **l** and **l′** are strongly coupled, leading to $\mathbf{l} \approx \mathbf{l}'$ or $\mathbf{l}_i \approx \mathbf{l}_i'$ for the ith vibrational pair[1,2]. The conservation of angular momentum dictates $\mathbf{J}_{total} = \mathbf{l} + \mathbf{j}_{CH4} = \mathbf{l}' + \mathbf{j}_{CH3} + \mathbf{j}_{HF}$. The initial rotational angular momentum of CH_4, $\mathbf{j}_{CH4}$, is negligibly small for a supersonically expanded beam at the rotational temperature of ∽8 K (ref. 43). Therefore, $\mathbf{j}_{CH3} + \mathbf{j}_{HF}$ must be small, in line with experimental finding of small rotational energy disposal of 1.5 kcal mol^{-1} (Method: Energy disposal) and 6D-QD results that both rotors exhibit low excitations with distributions peaking around $j \approx 2$ (Supplementary Fig. 4). Since $l' = m'u'b'$, where m' denotes the reduced mass of two products, u' is the recoiling speed and b' the impact parameter of the departing products. In a direct near-collinear scattering process, smaller b' tends to associate with smaller b, thus prefers backward scattering. In keeping with $\mathbf{l}_i' \approx \mathbf{l}_i$, a more exoergic product pair with faster speed u', e.g., (2_n, 1) or (0_0, 2), must recoil with smaller b', i.e., preferentially in the backward direction. Likewise, the channel recoiled with small translational energy, such as (0_0, 3), will be mostly forward-scattered. The key factor in governing this kinematic correlation between angle and orbital angular momentum seems to be the energetics—irrespective of product vibrational modes—in accord with the observed trend.

The above kinematic consideration, rooted in the A + BC reaction, should hold for the newly formed H–F bond (Supplementary Fig. 5). The CH_3-moiety is not directly involved in bond cleavage and formation. Yet, the mere fact that about 57% of total reactive fluxes are channeled into umbrella-excited CH_3 products attests to the strong coupling of the umbrella motions of CH_3 to the reaction coordinate; thus, CH_3-moiety is not an innocent spectator and cannot be regarded as a pseudo-atom. To understand the mechanistic origin of the observed umbrella-mode excitation and its dynamical attributes, we first note that the breaking C–H bond is always directed away from (and uniformly distributed around) the center-of-mass of CH_4, which lies on the C-atom. This site-specific consideration leads to the notion of peripheral dynamics[44,45] for the present reaction, whose transition-state features a reactant-like structure with elongated F–H bond and slightly distorted umbrella angles (∽107°) from the tetrahedral angle (109.5°) of CH_4[35,42].

For the large impact-parameter or high- l collisions (the grazing collisions), the force along the line-of-centers (i.e., the incident F-atom

https://doi.org/10.1038/s41467-025-66587-x

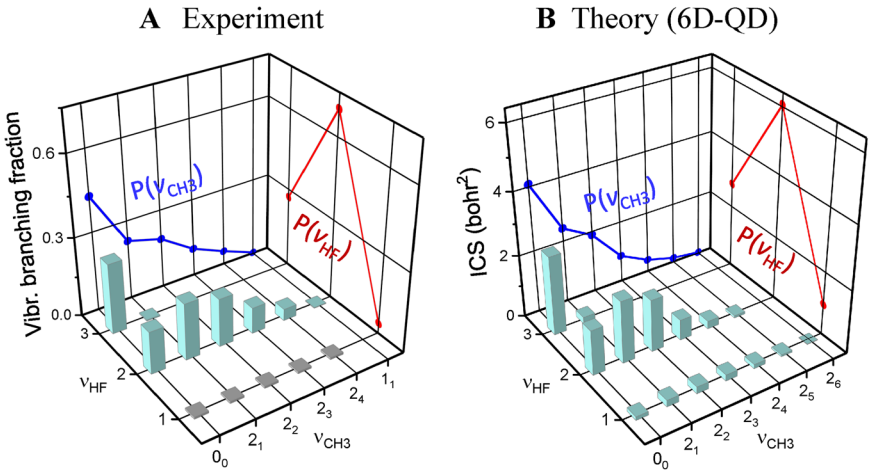

Fig. 3 | Comparison of (pair) correlated vibrational branching fraction in the (v_{CH3}, v_{HF}) matrix representation. A Experimental data were deduced directly from Fig. 2C, D—no need for any normalization factors; the total sum is unity, and **B** theoretical results are from a 6D quantum dynamics simulation on a highly accurate ab initio potential energy surface, including the effects of reactant rotational states (Supplementary Fig. 3). Both experiment and theory indicate the dominance of umbrella-mode of excitations of $CH_3(v_2)$. The previously reported anti-correlated excitation of two vibrators ($CD_3(v_2)$ and $DF(v)$) in the reaction of $F + CD_4$[13,15] is affirmed, but in a complete and more quantitative manner in the present case. The conventional (or uncorrelated) product state distributions of HF (in red) and $CH_3(v_i)$ (in blue) are displayed on the respective background, which are obtained by proper summation of state populations of the coproduct CH_3 and HF, respectively. Only very minor discrepancies can be noted. The overall agreements between experiment and theory are excellent. Experimental signals for the faster speed part, i.e., those for the formation of $HF(v=1)$, are very weak and featureless. Judging from the extent of its distribution, an evenly distributed pair population was tentatively posited as gray blocks.

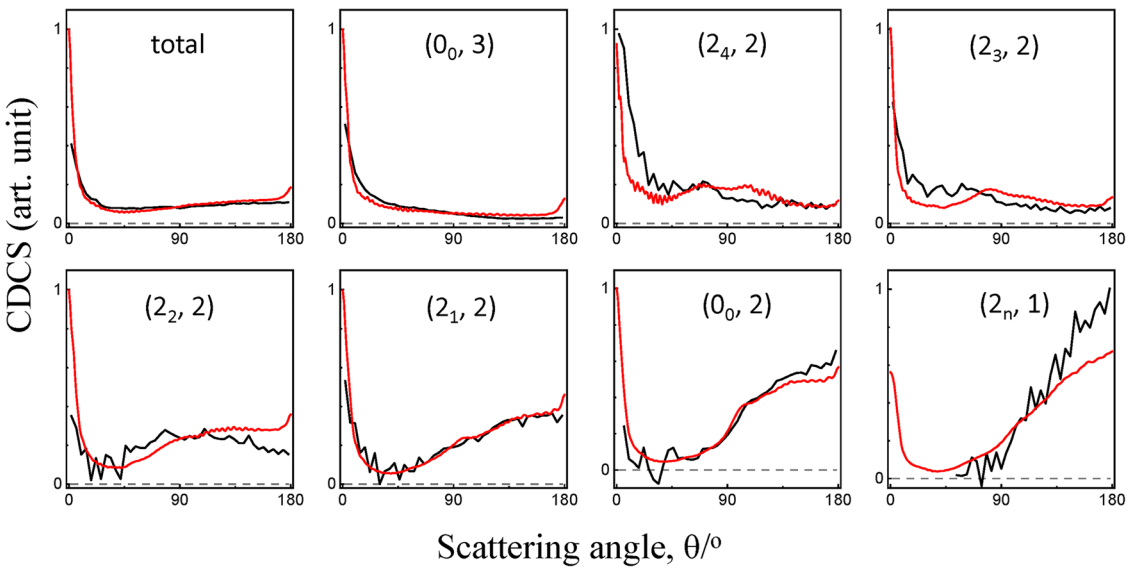

Fig. 4 | Comparison of correlated differential cross sections (CDCSs) of the prominent product pairs. Experimental CDCSs ($d\sigma/d\cos\theta$) are in black and theory in red. Supplementary Figs. 8, 9 detail the experimental procedures to retrieve the CDCSs from the overlapped image. Due to the enormous computational costs in 6D-QD, only the ground-state reaction with $CH_4(v=0, j=0)$ was calculated. Including the rotationally excited $CH_4(j=1$ and 2) would reduce the contributions from the resonance-mediated pathway (evidenced by Supplementary Fig. 3), thus likely suppressing both the prominent forward and minute backward peaks. "Total" denotes the overall angular distribution, which includes all minor product channels; experimentally, it was deduced directly from the density-to-flux corrected image. Since only the shapes are of concern, experiment and theory in each panel are normalized to the same fluxes (i.e., integration of $(d\sigma/d\cos\theta)\cdot\sin\theta$ over all angles θ).

to the C-atom) will be weak, exerting little distortion to the reactant-like transition-state structure. As the H-atom is abstracted with vibrational-excited HF scattered forward, the pyramidal CH_3-moiety at transition state flattens abruptly to the planar CH_3 product structure, resulting in mildly umbrella-excited CH_3 products. On the other hand, for the low- l collisions (the head-on collisions), the line-of-centers force imparted by the incident F-atom is stronger, which attracts a H-atom under attack, causing the remaining CH_3-moiety flattened gradually until the rupture of attacked C–H bond, and thus leads predominantly to the backward-scattered ground-state CH_3 products. This qualitatively explains the observed correlation that low umbrella-excited CH_3 prefers backward scattering, whereas higher umbrella-excited CH_3 yields more in the sideway and forward directions. A theoretical inspection on how the umbrella motion of CH_3-moiety evolves along the reaction path (Supplementary Fig. 6) confirms this classical physical picture.

It is worth noting that the proposed interpretation can also account for a recently reported center-barrier reaction of $D + CH_4$

(ref. 46) and H + CH_4/CD_4 (ref. 47). where the umbrella angle at the transition state is 103° (ref. 48). Hence, like the present reaction, the ground state-pair (0_0, 0) is expected to be scattered more backward than the umbrella-excited pair (2_1, 0), as experimentally observed. More elaborative QD wave-packet analysis led to the same conclusion[46]. As for the reversed behavior in the late-barrier Cl + CH_4 reaction, i.e., the ground state CH_3 products tend to be scattered more in the forward hemisphere (Supplementary Fig. 7), it can again be comprehended within this angle-angular momentum correlation framework. This is because that compared to the low- l collisions, the high- l collisions induce weaker distortion to the product-like transition-state structure, which features a nearly planar CH_3-moiety; leading to more forward-scattered ground-state CH_3 products. Putting together, with the consideration of the entire transition-state structure (meaning both the active X–H–C site and the spectator CH_3 moieties), this angle-angular momentum correlation provides a conceptually appealing framework for understanding diverse dynamic behaviors of a host of direct reactions. The mechanistic insight proposed here in turn serves as a vivid example to illustrate how the product dynamical attributes are controlled by the transition-state structure[49].

Discussion

All molecules can be photoionized with either known or readily computable one-photon ionization cross sections in the VUV regime. This general-purpose ionization probe can be transformed into a universal detection with the product state-resolved capability—the best of two worlds. Traditional universal detection measures the neutral product speed distribution; thus, the finite scattering and ionization volumes limit its resolution. This limitation can be mitigated, however, by interrogating instead the photoionized products at collision center in harness with a 3D-VMI scheme. Compared to the widely used REMPI-tagged imaging approach, the current approach is less efficient in ionization for its non-resonant nature, and intrinsically of lower state-resolving power (because all internal states will be ionized with recoiled energies inevitably intertwined in the total translational energy measurement), and is prone to photochemical background problems due to its universal ionization. Nonetheless, those obstacles could be overcome and out came the results that provide a complete (rather than fragmentary) and more robust dynamical information from a single image measurement.

As demonstrated here, the dynamics of F + CH_4 reaction are uncovered in full, showing merely 40% of reactivity yielding the ground-state CH_3 products, despite being the most prominent feature in the REMPI spectra. Most reactive fluxes are instead channeled into umbrella-excited CH_3 with little or negligible amounts for three other vibrational modes. The capability of both universal and state-specific detections at the same time also enables us to pinpoint the angle-angular momentum correlation being the underlying mechanism for the observed vibrationally state-dependent angular distributions. The same correlation can also account for the diverse behaviors reported in the literatures on a family of X + CH_4 reactions. Comparisons with concurrent 6D-QD calculations on both pair-correlated vibrational branching and state-resolved angular distributions show excellent agreements in nearly all aspects, testifying the reliability of the proposed experimental method. Hence, complementary to the established detection methods, a new approach that captures the essential traits of all existing methods is now added to the experimentalist's toolbox. It should be particularly well-suited for investigating complex multi-channel processes by providing otherwise inaccessible insights as well as illuminating a clear roadmap for more detailed studies.

Methods

Experiment

Supplementary Fig. 1 depicts the crossed-beam setup used in this work[12,50,51]. It consisted of two rotatable pulsed molecular beams and a fixed detector assembly housed in a vacuum chamber. The F-atom beam was generated by a pulsed high-voltage discharge of 5% F_2 seeded in a pulsed supersonic expansion of Ne at 6 atm. The CH_4 beam was also produced by pulsed supersonic expansion of neat CH_4 at 6 atm and characterized by a rotational temperature of 8 K, i.e., the initial j-state distribution of $n_{j=0}$: $n_{j=1}$: $n_{j=2}$ = 0.31: 0.54: 0.15 (ref. 43). Both beams were collimated by double skimmers and crossed in a differentially pumped scattering chamber; collision energy (E_c) was tuned by varying the intersection angle of the two molecular beams. To interrogate the reaction products, non-resonant one-photon ionization of CH_3 radicals was employed using 118 nm photon that was produced by the third harmonic generation scheme of a third harmonics YAG laser (355 nm) in a cell filled with ~11 Torr of Xe (ref. 50). The CH_3^+ thus generated was then guided by a set of specially designed ion-optics and velocity-mapped in a three-dimensional manner onto the image detector consisting of gated-MCP, phosphor, and CCD camera[12,51]. The center-sliced image was then recorded by a computer for data analysis (Supplementary Fig. 2).

Image analysis

To retrieve the state-resolved angular distributions, or the CDCSs, from the overlapped image features, a two-step data analyses were performed. First, we tested how each individual CDCS will be affected by the sampling annulus with different widths or the u-ranges. As shown in Supplementary Fig. 8 samplings of three different annular widths (the right panels) exert little effect on the resultant CDCSs (the left panels). With that, we then proceeded to disentangle the "contaminations" from the proximate peaks for each given product pair to recover the 'best-estimated' CDCS. Based on the red-shaded slabs in the right-middle panel in Supplementary Fig. 8 for the respective product pair, we analyzed the angular distribution over the corresponding u-range. The results are presented as the black line in Supplementary Fig. 9, which encompasses both the desired distribution and the contamination from the adjacent product pairs. Due to the asymmetric P_u profiles, the position and width of each desired pair were chosen so that it would capture its main peak with contaminations mainly from the lower speed part of the adjacent pair to the right and the long tail of the (0_0, 2) pair. The extent of contamination can be estimated from the overlapped flux or the area. Starting from the right, (0_0, 2), the overlap-corrections were then performed progressively one-by-one towards the left. The results are presented as the red lines in Supplementary Fig. 9, which represent our "best-estimated" CDCSs. Tests were also performed for somewhat different choices of u-slabs to ensure the consistency of the results.

Energy disposal

Conservation of energy can be expressed as $E_{total} = -\Delta H_{rx} + E_c = V_{(CH3+HF)} + R_{(CH3+HF)} + T_{(CH3-HF)}$, where ΔH_{rx} is the heat of reaction (–31.82 kcal mol^{-1}), $V_{(CH3+HF)}$ (or $R_{(CH3+HF)}$) denotes the averaged energy deposited into two product vibrators (or rotors), and $T_{(CH3-HF)}$ is the averaged kinetic energy release of the departing products. Experimentally, the product speed distribution was measured; thus $T_{(CH3-HF)}$ can be deduced from Fig. 2D, 6.1 kcal mol^{-1} or a fractional translational energy release f_T = 0.178. The vibrational energy disposal $V_{(CH3+HF)}$ can be derived from the normalized pair-correlated distribution presented in Fig. 3A, $V_{(CH3+HF)}$ = 26.7 kcal mol^{-1} or f_V = 0.778. Notably, most of the available energy is deposited into the vibrational motions of the newly formed HF bond ($f_{V(HF)}$ = 0.71), in line with Polanyi's rule for a highly exoergic atom + diatom reaction with an early barrier[4]. The conservation of energy, $f_T + f_V + f_R = 1.0$, will then lead to f_R = 0.044 or a low value of 1.5 kcal mol^{-1} for the combined energies of two rotors $R_{(CH3+HF)}$. In view of relatively large rotational constants of two products (B_{CH3} ~9.6 cm^{-1}, C_{CH3} ~4.7 cm^{-1}, and B_{HF} ~ 19 cm^{-1}), small values of $j_{CH3} + j_{HF}$ are then expected.

Theory: Reduced dimensional state-to-state quantum dynamics calculation

The reduced dimensional model employed in the time-dependent wave packet (TDWP) calculations here was the free-torsion seven-dimensional (FT-7D) model we proposed for the $X + YCZ_3 \rightarrow XY + CZ_3$ reaction in 2013 (ref. 34), by assuming that the CZ_3 group can rotate freely with respect to its C_{3V} symmetry axis (Supplementary Fig. 10). With the bond length of CH fixed at its equilibrium value in reactant (2.06 bohr) because it essentially does not change during the reaction, the number of the degrees of freedom included in the calculation was reduced to six. We used the multiple-step reactant–product decoupling (MRPD) method[52,53] to obtain the state-to-state information. We carried out state-to-state calculations covering all the total angular momentum J_{total} from 0 to 60 to converge the ICS and DCS for the initial ground state reaction for collision energies up to 0.1 eV. The state-to-state ICS for the initial CH_4 rotational excitation were obtained using the weight-inclusive J-shifting method[41], by including results for $J_{total} = 0$, 20, 40, and 60. The impacts of reactant rotations to CICSs are summarized in Supplementary Fig. 3.

Numerical parameters used in the 6D-QD calculation

The numerical parameters used in reactant Jacobi coordinates are as following: A total number of 280 sine basis functions covering a range from 3.0 to 19.8 bohrs were used for R with 110 grid points in the interaction region. For the r dimension, 70 basis functions were used in the range of [1.0, 9.0] bohrs in the interaction region, while six basis functions were used in the asymptotic region. The number of basis functions for the umbrella motion was 16. The rotational basis functions were constrained by the parameters, $J_{max} = 164$, $l_{max} = 140$, $j_{max} = 24$. The center of the prepared Gaussian wave packet was located at $R_0 = 18.0$ bohrs, with the width of δ=0.2 bohr, and the central energy of $E_0 = 0.15$ eV. For total angular momentum $J_{total} = 0$, we propagated the wave packets for 150,000 a.u. of time with a time step of 10 to converge the reaction probabilities. The absorption potential on the r coordinate for the MRPD calculation takes the form

$$V_p(r) = C\left(\frac{r - r^0}{\Delta r}\right)^n,$$

with $r^0 = 6.5$ a.u., Δr=2.5 a.u., $C = 0.04$, and $n = 1.5$. To minimize the computational cost, the coordinate transformation is carried out at every eight propagation time steps. Continuous propagation in the product Jacobi coordinates only involves a total number of 300 sine functions for the translational coordinate in a range of [3.0, 21.0] bohrs and seven vibrational basis functions for HF bond. The number of basis functions for the umbrella motion was 11. The rotational basis functions were constrained by the parameters, $J'_{max} = 54$, $l'_{max} = 30$, and $j'_{max} = 24$. A dividing surface is placed at $R' = 15.5$ bohr to extract S matrix elements. The number of K'-blocks included in the product calculation increases with the total angular momentum, from 1 for $J_{total} = 0$, up to 7 for $J_{total} = 60$.

Data availability

All data in the main text and the supplementary information are available at https://figshare.com/s/c2ae0cd070ae2b583cd8. Source data are provided with this paper.

References

1. Levine, R. D. & Bernstein, R. B. *Molecular Reaction Dynamics and Chemical Reactivity* (Oxford Univ. Press, 1987).
2. Brouard, M. & Vallance, C. (eds) *Tutorials in Molecular Reaction Dynamics* (Royal Society Chemistry, 2010).
3. Herschbach, D. R. Molecular dynamics of elementary chemical reactions (Nobel Lecture). *Angrew. Chem. Int. Engl. Ed.* **26**, 1221–1243 (1987).
4. Polanyi, J. C. Some concepts in reaction dynamics. *Science* **236**, 680–690 (1987).
5. Lee, Y. T. Molecular beam studies of elementary chemical processes. *Science* **236**, 793–798 (1987).
6. Pan, H., Liu, K., Caracciolo, A. & Casavecchia, P. Crossed beam polyatomic reaction dynamics: recent advances and new insights. *Chem. Soc. Rev.* **46**, 7517–7547 (2017). and references therein.
7. Kaiser, R. I. & Mebel, A. M. On the formation of polyacetylenes and cyanopolyacetylenes in Titan's atmosphere and their role in astrobiology. *Chem. Soc. Rev.* **41**, 5490–5501 (2012).
8. Li, H. & Suits, A. G. Universal crossed beam imaging studies of polyatomic reaction dynamics. *Phys. Chem. Chem. Phys.* **22**, 11126–11138 (2020).
9. Proctor, D. L. & Davis, H. F. Vibrational vs. translational energy in promoting a prototype metal–hydrocarbon insertion reaction. *Proc. Natl Acad. Sci. USA* **105**, 12673–12677 (2008).
10. Lee, S.-H., Chen, W.-K. & Huang, W.-J. Exploring the dynamics of reactions of oxygen atoms in state ^{3}P and ^{1}D with ethane at collision energy 3 kcal mol^{-1}. *J. Chem. Phys.* **130**, 054301 (2009).
11. Neumark, D. M., Wodtke, A. M., Robinson, G. N., Hayden, C. C. & Lee, Y. T. Molecular beam studies of the F + H_2 reaction. *J. Chem. Phys.* **82**, 3045–3066 (1985).
12. Lin, J. J., Zhou, J., Shiu, W. & Liu, K. Application of time-sliced ion velocity imaging to crossed molecular beam experiments. *Rev. Sci. Instrum.* **74**, 2495–2500 (2003).
13. Lin, J. J., Zhou, J., Shiu, W. & Liu, K. State-specific correlation of coincident product pairs in the F + CD_4 reaction. *Science* **300**, 966–969 (2003).
14. Liu, K. Product pair correlation in bimolecular reactions. *Phys. Chem. Chem. Phys.* **9**, 17–30 (2007).
15. Zhou, J., Lin, J. J., Shiu, W. & Liu, K. State-correlation matrix of the product pair from F + CD_4 → DF(v') + CD_3(0 v_2 0 0). *Phys. Chem. Chem. Phys.* **8**, 3000–3006 (2006).
16. Shu, Y. et al. Vibrational state-resolved differential cross sections of the F + CH_4→ HF + CH3 reaction at the collision energies of 3.1–13.8 kcal/mol. *J. Phys. Chem. A* **128**, 9947–9954 (2024).
17. Eppink, A. T. J. B. & Parker, D. H. Velocity map imaging of ions and electrons using electrostatic lenses: application in photoelectron and photofragment ion imaging of molecular oxygen. *Rev. Sci. Instrum.* **68**, 3477–3484 (1997).
18. Wiley, W. C. & McLaren, I. H. Time-of-flight mass spectrometer with improved resolution. *Rev. Sci. Instrum.* **26**, 1150–1157 (1955).
19. Wang, J.-H., Hsu, Y.-T. & Liu, K. Photodissociation dynamics of C_2H_2, C_2D_2, and C_2HD at 121.6 nm. *J. Phys. Chem. A* **101**, 6593–6602 (1997).
20. Parker, J. H. & Pimentel, G. C. Vibrational energy distribution through chemical laser studies. I. Fluorine atoms plus hydrogen or methane. *J. Chem. Phys.* **51**, 91–96 (1969).
21. Moore, C. M., Smith, I. W. M. & Stewart, D. W. A. Rates of processes initiated by pulsed laser production of F atoms in the presence of HCl, CH_4, and CF_3H. *Int. J. Chem. Kinet.* **26**, 813–825 (1994).
22. Persky, A. Kinetics of the F + CH_4 reaction in the temperature range 184–406 K. *J. Phys. Chem.* **100**, 689–693 (1996).
23. Wickramaaratchi, M. A., Setser, D. W., Hildebrandt, H., Korbitzer, B. & Heydtmann, H. Evaluation of HF product distributions deduced from infrared chemiluminiscence. II. F atom reactions. *Chem. Phys.* **94**, 109–129 (1985).
24. Nazar M. A. & Polanyi J. C. Energy distribution among reaction products. XIV. F + CH_4, F + CH_3X(X = Cl, Br, I), F + CH_nCl_{4-n}(n = 1–3). *Chem. Phys.* **55**, 299-311 (1981).
25. Harper, W. W., Nizkorodov, S. A. & Nesbitt, D. J. Quantum state-resolved reactive scattering of F + CH_4 → HF(v, j) + CH_3: nascent HF(v. j) product state distributions. *J. Chem. Phys.* **113**, 3670–3680 (2000).

26. Sugawara, K., Ito, F., Nakanaga, T., Takeo, H. & Matsumura, C. Vibrational and rotational energy distributions of CH_3 and IF formed in the reactions of F atoms with CH_4 and CH_3I. *J. Chem. Phys.* **92**, 5328–5337 (1990).
27. Corchado, J. C. & Espinosa-Garcia, J. Theoretical study of the CH_4 + F → CH_3 + FH reaction. I. Ab initio reaction path. *J. Chem. Phys.* **105**, 3152–3158 (1996).
28. Taatjes, C. A. et al. Absolute photoionization cross-section of the methyl radical. *J. Phys. Chem. A* **112**, 9336–9343 (2008).
29. Gans, B. et al. Determination of the absolute photoionization cross sections of CH_3 and I produced from a pyrolysis source, by combined synchrotron and vacuum ultraviolet laser studies. *J. Phys. Chem. A* **114**, 3237–3246 (2010).
30. Aguirre, F. & Pratt, S. T. Photoionization of vibrationally hot CH_3 and CF_3. *J. Chem. Phys.* **122**, 234303 (2005).
31. Gardiner, S. H., Lipciuc, M. L., Karsili, T. N. V., Ashfold, M. N. R. & Vallance, C. Dynamics of the A-band ultraviolet photodissociation of methyl iodide and ethyl iodide via velocity-map. *Phys. Chem. Chem. Phys.* **17**, 4096–4106 (2015).
32. Shiu, W., Lin, J. J., Liu, K., Wu, M. & Parker, D. H. Imaging the pair-correlated excitation function: The F + CH_4 → HF(v') + CH_3(v=0). *J. Chem. Phys.* **120**, 117–122 (2004).
33. Shiu, W., Lin, J. J. & Liu, K. Reactive resonance in a polyatomic reaction. *Phys. Rev. Lett.* **92**, 103201 (2004).
34. Liu, S., Chen, J., Zhang, Z. & Zhang, D. H. A six-dimensional state-to-state quantum dynamics study of the H + CH_4 → H_2 + CH_3 reaction (J = 0). *J. Chem. Phys.* **138**, 011101 (2013).
35. Chen, J., Xu, X., Liu, S. & Zhang, D. H. A neural network potential energy surface for the F + CH_4 reaction including multiple channels based on coupled cluster theory. *Phys. Chem. Chem. Phys.* **29**, 9090–9100 (2018).
36. Palma, J. & Clary, D. C. A quantum model Hamiltonian to treat reactions of the type X+YCZ_3→XY+CZ_3: Application to O(^{3}P) +CH_4→OH+CH_3. *J. Chem. Phys.* **112**, 1859–1867 (2000).
37. Aoiz, F. J. et al. Classical dynamics for the F + H_2 → HF + H reaction on a new ab initio potential energy surface. A direct comparison with experiment. *Chem. Phys. Lett.* **223**, 215–226 (1994).
38. Liu, K. Quantum dynamical resonances in chemical reactions: from A+BC to polyatomic systems. *Adv. Chem. Phys.* **149**, 1–46 (2012).
39. Zhou, J., Lin, J. J. & Liu, K. Observation of a reactive resonance in the integral cross section of a six-atom reaction: F+CHD_3. *J. Chem. Phys.* **121**, 813–818 (2004).
40. Zhou, J., Lin, J. J. & Liu, K. Deciphering the nature of the reactive resonance in F + CHD_3: correlated differential cross-sections of the two isotopic channels. *Mol. Phys.* **108**, 957–968 (2010).
41. Liu, S., Chen, J., Zhang, X. & Zhang, D. H. Feshbach resonances in the F + CHD_3 → HF + CD_3 reaction. *Chem. Sci.* **14**, 7973–7979 (2023).
42. Czako, G., Shepler, B. C., Braams, B. J. & Bowman, J. M. Accurate ab initio potential energy surface, dynamics, and thermochemistry of the F + CH_4 → HF + CH_3 reaction. *J. Chem. Phys.* **130**, 084301 (2009).
43. Chen, Y., Pan, H., Wang, F. & Liu, K. On the signal depletion induced by stretching excitation of methane in the reaction with the F atom. *Phys. Chem. Chem. Phys.* **16**, 444–452 (2014).
44. Valentini, J. J. Mapping reaction dynamics via state-to-state measurements:rotations tell the tale. *J. Phys. Chem. A* **106**, 5745–5759 (2002).
45. Kornweitz, H., Persky, A. & Levine, R. D. The exoergic F + CH_4 reaction as an example of peripheral dynamics. *Chem. Phys. Lett.* **289**, 125–132 (1998).
46. Tan, Y. et al. Revealing umbrella bending as a reporter mode in the D + CH_4 reaction. *Nat. Commun.* **16**, 5893 (2025).
47. Chen, W. et al. Crossed molecular beam study of H + CH_4 and H + CD_4 reactions: vibrationally excited CH_3/CD_3 product channels. *Chin. J. Chem. Phys.* **30**, 609–613 (2017).
48. Wu, T., Werner, H.-J. & Manthe, U. Accurate potential energy surface and quantum reaction rate calculations for the H + CH_4 → H_2 + CH_3 reaction. *J. Chem. Phys.* **124**, 164307 (2006).
49. Guo, H. & Liu, K. Control of chemical reactivity by transition-state and beyond. *Chem. Sci.* **7**, 3992–4003 (2016).
50. Wang, P. et al. Unraveling the photodissociation branching and pathways of methane at 118 nm by imaging the CH_3, CH_2, and CH fragments. *J. Phys. Chem. A* **128**, 5273–5284 (2024).
51. Pan, H. & Liu, K. Fermi-phase-induced interference in the reaction between Cl and vibrationally excited CH_3D. *Nat. Chem.* **14**, 545–549 (2022).
52. Liu, S., Xu, X. & Zhang, D. H. Time-dependent wave packet theory for state-to-state differential cross sections of four-atom reactions in full dimensions: application to the HD + OH → H_2O + D reaction. *J. Chem. Phys.* **136**, 144302 (2012).
53. Chen, Z. et al. Reactivity oscillation in the heavy–light–heavy Cl + CH_4 reaction. *Proc. Natl. Acad. Sci. USA* **117**, 9202–9207 (2020).

Acknowledgements

This work was supported by the National Natural Science Foundation of China (Grants Nos. 22373047 (H.P.), 22573104 (S.L.), and 22288201 (D.H.Z.)); Guangdong Introduced Innovative R&D Team Project grant 2019ZT08L455 (X.Y. and H.P.); the Strategic Priority Research Program of the Chinese Academy of Sciences (Grant Nos. XDB0450202 (S.L.), XDB0970200 (D.H.Z.)); the Innovation Program for Quantum Science and Technology (Grant No. 2021ZD0303305 (D.H.Z.)); the open fund (SKLMRD-K202523) of the State Key Laboratory of Chemical Reaction Dynamics in DICP, CAS (H.P.); and the Liaoning Revitalization Talents Program (Grant No. XLYC2203062 (S.L.)).

Author contributions

H.P. and K.L. conceived and designed the experiments. H.P. and P.W. performed the experiments; H.P. analyzed the data. S.L. and D.H.Z. performed theoretical calculations. K.L., D.H.Z., and X.Y. supervised the project. H.P wrote the initial manuscript with the inputs from all authors. S.L. wrote the theoretical sections. K.L., D.H.Z., and X.Y. reviewed and edited the manuscript.

Competing interests

The authors declare no competing interests.

Additional information

Supplementary information The online version contains supplementary material available at https://doi.org/10.1038/s41467-025-66587-x.

Correspondence and requests for materials should be addressed to Huilin Pan, Shu Liu, Xueming Yang or Dong H. Zhang.

Peer review information *Nature Communications* thanks Hong Gao, and the other, anonymous, reviewer(s) for their contribution to the peer review of this work. A peer review file is available.